Drag and Total Pressure Distributions in Scramjet Engines at Mach 8 Flight

Tohru Mitani* and Tetsuo Hiraiwa[†]
National Aerospace Laboratory, Kakuda, Miyagi 981-1525, Japan
and
Yuichi Tarukawa[‡] and Goro Masuya[§]
Tohoku University, Sendai, Miyagi 980-0845, Japan

To complement our hydrogen-fueled scramjet engine research, aerodynamic tests were conducted by using one-fifth-subscaled (0.44 m-long) models in Mach 6.7 freestream conditions. The drag of the engines was estimated by using a force balance and pressure distributions on the internal wall to separate the internal drag and the external drag. The swept shock wave theory yielded the air capture ratio and the additive drag due to the spilled flow. Two methods for drag evaluation, based on force balance measurement and on wall pressure Pw measurement, were compared to examine their accuracies. They enable identifying the origins of pressure and friction drags. It was found that frictional drag constituted more than half of the internal drag of engines and that the pressure recovery across the engine decreased to about 4% when large struts were installed in the inlets. The fundamental principles and the experimental validation of the methods for evaluating the internal drag in scramjet engines with large struts is reported.

Nomenclature

A	=	cross-sectional area
A_{cap}	=	engine air capture area
A_{duct}	=	spilled flow area, $(A_1 - A_{cap})$
A_{wet}	=	wetted area by spilled flow on sidewalls (Fig. 2)
C_{add}	=	coefficient of additive drag due to spilled flow, defined based on q_1 and A_1
C_{duct}	=	drag coefficient on engine duct flow, $(C_{int} - C_{add})$
C_{ext}	=	drag coefficient on engine external wet surfaces
C_{FMS}	=	drag coefficient of engine measured by force measuring system, $(C_{int} + C_{ext} + C_0)$
C_{int}	=	engine internal drag coefficient including C_{add}
C_0	=	drag coefficient of top wall and the model support
Cd_f	=	frictional drag coefficient
Cd_p	=	pressure drag coefficient
c_f	=	wall friction coefficient
H	=	height of engine inlets
H_s	=	height of dividing streamline
h_s	=	H_s/H
h_1	=	δ_1/H
h_2	=	δ_2/H
L	=	length of engines
M	=	Mach number
P	=	static pressure
P^0	=	total pressure
Pw	=	wall pressure inside of engines
q	=	dynamic pressure
Re	=	local Reynolds number
T	=	static temperature
T^0	=	total temperature
u	=	flow velocity
W	=	width of inlet where $A_1 = H \times W$
x	=	streamwise distance from inlet leading edge
y	=	distance from the top wall
z	=	spanwise distance in engines
γ	=	specific heat ratio
δ	=	99% velocity boundary-layer thickness
δ_1	=	displacement thickness in boundary layer
δ_2	=	momentum thickness in boundary layer
ε_i	=	contraction ratio in internal flow, A_i/A_1
η_c	=	air capture ratio in inlets, $(H_s - \delta_1)/(H - \delta_1)$
η_p	=	recovery ratio in total pressure
η_{T0}	=	total temperature ratio T_i^0/T_1^0
θ	=	deflection angle
τ_w	=	wall shear stress in engine ducts

Subscripts

1	=	entrance of inlets
2	=	exit of inlets
3	=	plane with complete mixing of fuel (upstream of the backward-facing step: the throat of engines)
4	=	entrance of combustors
5	=	exit of engines

Introduction

HYDROGEN-FUELED scramjet engines are tested in our RamJet Engine Test Facility under Mach 4, 6, and 8 flight conditions. The comprehensive research activities are summarized in Ref. 1. The scramjet engine is rectangular with a length of 2.2 m and consists of a cowl, a top wall, and two sidewalls. The sidewall compression-type inlet consists of 6-deg wedges, the leading edges of which are swept back by 45 deg to deflect the airstream to achieve suitable spillage for engine starting. Thrust increment overcoming the engine drag was observed in the Mach 4 and Mach 6 tests. The test results in the Mach 6 tests and the latest testing at the Mach 8 condition are reviewed in Refs. 2–4.

The thrust increment due to combustion provides combustion performance of the engines. The net thrust in the ramjet engines, however, is defined as the thrust increment minus engine drag, where the engine drag is measured as no-fuel engine internal drag. For instance, an increase in the engine compression ratio improves the combustion performance. The increased compression ratio also increases the engine drag and may result in deterioration of the engine net thrust. In addition to the improvement of the combustion performance, minimization of the engine drag is essential to maximize net thrust performance.

However, data on drag measurements in scramjet engines are limited. A comparative study of engine performance assessment has been conducted based on energy and thrust potential for a simplified engine.[5] However, there is no quantitative evaluation on irreversible processes in engines. Some fuel-off engine drag data have been reported by Guy et al. for a scramjet engine tested in the NASA Langley Research Center Mach 7 (the freejet Mach number 6.08) Arc-Heated Test Facility.[6] To optimize the internal geometry, losses in engine internal flow should be itemized and quantified. The internal drag and additive drag should be separated to enable discussion of the internal flow properties. Voland[7] proposed three methods to determine the internal drag. He applied them to a strutless parametric engine of the NASA Langley Research Center to $C_{int} = 0.150$ in a Mach 6 stream. Mitani et al.[8] measured the engine drag by a force balance and the wall pressure distribution in engines in a Mach 3.4 freestream. Mitani et al.[9] proposed a method to evaluate the additive drag due to the spilled flow and extended the methods for determining the total pressure through engine ducts. Recently, theoretical combustion and net thrust performance of scramjet engines have been calculated based on such internal aerodynamic data.[10]

The intent of this paper is to demonstrate methods for evaluation of the internal aerodynamics in scramjet engines. First, subscale wind-tunnel tests are described to evaluate the engine internal drag. Then, a one-dimensional flow analysis enables relating the internal drag and the total pressure loss in engines. In addition to the force balance measurement, our wall pressure measurement yields the pressure drag and the friction drag on the engine internal walls. The sum of those drags yields the other internal drag, which should be compared with that obtained from the force balance. The consistency between these methods is discussed, and the breakdowns of the internal and the external drags, the pressure and the friction drags, and the origins of these drags are presented.

Measurements of Engine Internal Flow

Subscale Wind Tunnel: Models and Measurements

The wind tunnel used is a freejet type at a scale of exactly one-fifth of the RJTF engine wind tunnel, which has a square nozzle exit, 102×102 mm. Because the freestream is compressed by the bow shock waves in front of the fuselages, the Mach 8 aerodynamic tests were carried out by using one-fifth subscaled models of the RJTF engines in the Mach 6.7 freestream with $T^0 = 600$ K and $P^0 = 7$ MPa. The stagnation condition provided a Reynolds number of 2×10^6 with respect to the model height.

Two basic engine geometries were chosen in these subscale tests. The original engine (E1)[2] had a swept-back angle of 45 deg throughout the engine. When gas sampling measurement was made, severe distortion of air and fuel flows was found in the E1 engine.[3] To minimize the distortion of the airflow into the combustor, the swept-back angle of 45 deg was eliminated from the combustor to the nozzle exit in a new engine (E2).[4] Experimental results with the E2 engine are presented here.

Figure 1 is a photograph of the one-fifth subscaled model of E2 mounted on a force measuring system (FMS). It was designed to reproduce the internal and the external geometries so that the drag and the wall pressure Pw distributions were measured simultaneously. The model was instrumented with pressure taps at about 150 locations (typically 100 on the sidewall, 27 on the top wall, 10 on the cowl and 10 on the struts). The Pw distributions on the inner walls were measured by using three mechanical pressure scanners. All of the pressure tubing is hidden inside of the side walls. The air temperature was monitored at the facility nozzle exit and the engine exit to estimate the heat loss in the models.

Ground testing of scramjet engines should simulate the ingestion of boundary layers developed on the vehicle forebody. To examine the boundary layer entering the inlet, boundary-layer trips made of
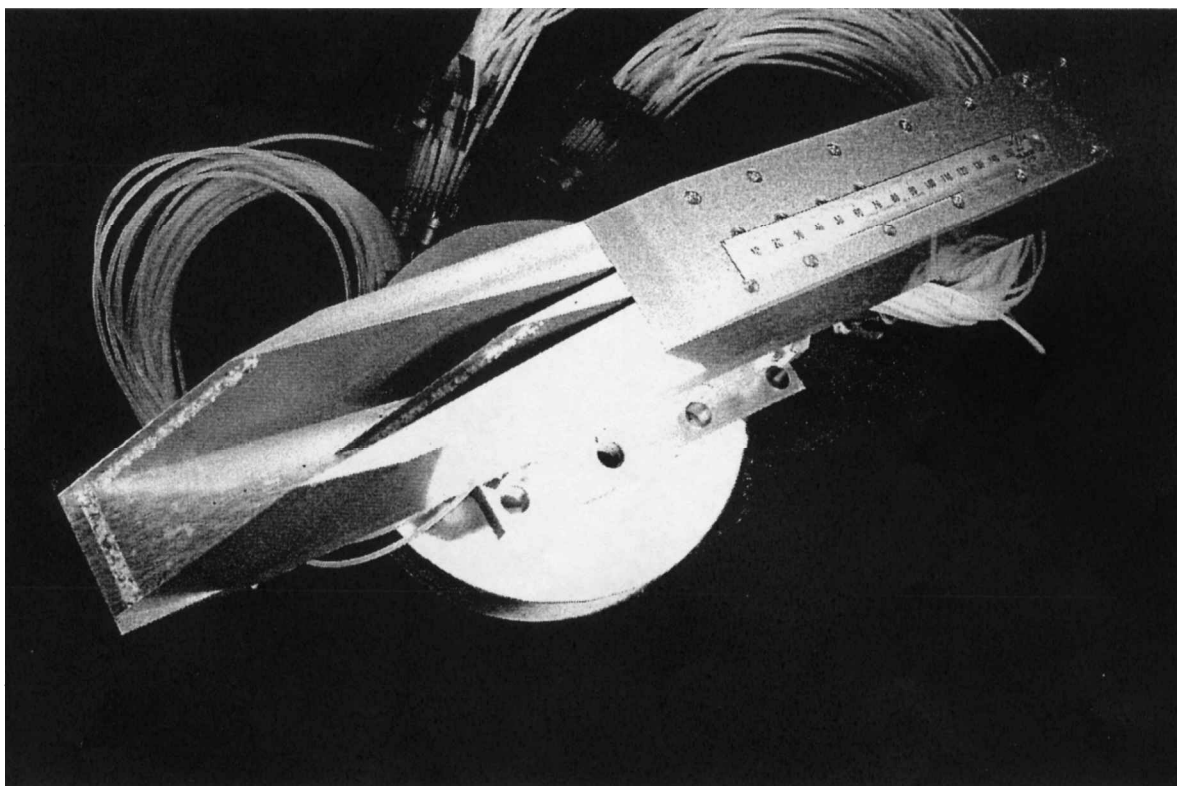

Fig. 1   Subscaled engine model: 40 mm wide, 50 mm high, and 440 mm long.
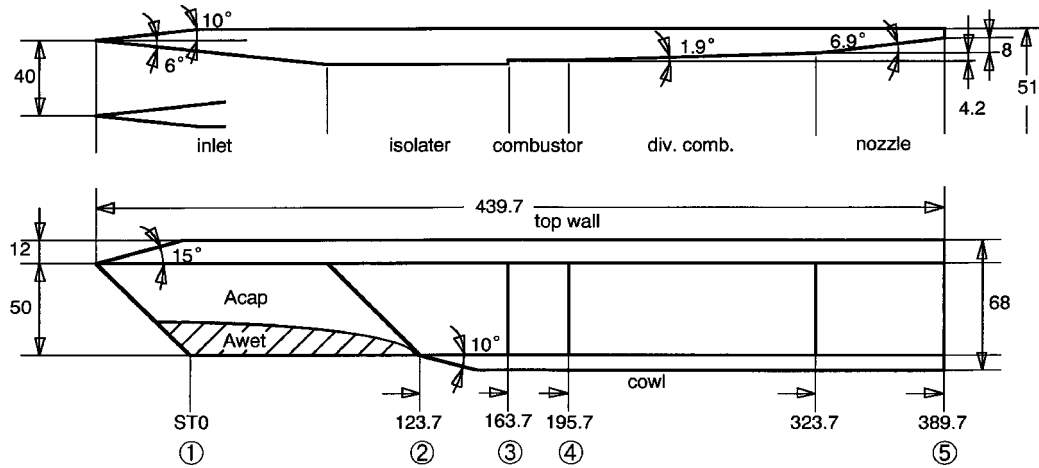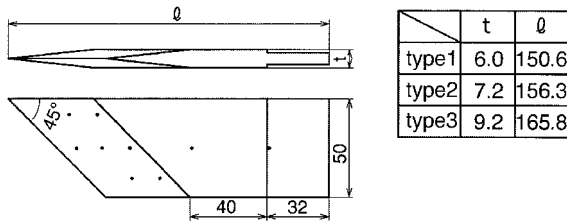
Fig. 2   One-fifth subscale model (in millimeter) and control surfaces; capture area A_{cap} and wet area on the sidewall with the spilled flow, A_{wet}, defined.
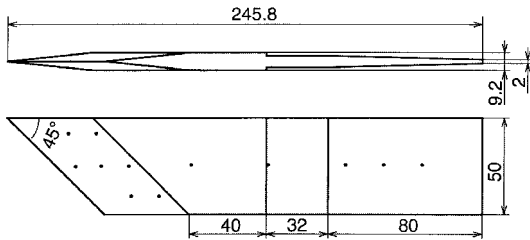

Fig. 3   Flameholding struts installed in the engine (in millimeter); contraction ratios summarized in Table 1.

Al_2O_3 grits are attached to the sidewalls and the topwall in Fig. 1. By the examination of the effects of the grits to Pw and unstart characteristics, the boundary layer in the models was concluded to be turbulent regardless of the grit. The models were suspended in the wind tunnel such that the top walls were aligned with the upper nozzle wall. The 99% velocity and the displacement thicknesses of the nozzle boundary layer were 15 and 7.9 mm, respectively. The boundary-layer ingestion sometimes promoted inlet unstart in the models with large struts. No significant effects on Pw and drag were observed in the Mach 6.7 tests.

Details of the model geometry are given in Fig. 2. In Fig. 2, control surfaces for the internal flows are also defined for the one-dimensional analysis. The entrance of the inlet with a cross-sectional area of 40×50 mm ($=A_1$) is assigned as station 1, and its exit is at station 2. A portion of the incoming air is spilled out from the inlet between stations 1 and 2. The isolator is located between stations 2 and 3. Station 3 corresponds to the upstream section of the backward-facing step (throat section with a minimum cross section). The entrance of the combustor behind the backward-facing step is located at station 4. The exit of the engine is at station 5.

This model was tested with various flameholding struts shown in Fig. 3. Four struts without the swept-back angle in the trailing edge were employed to minimize the air distortion downstream of models. The half apex angle of the leading wedges of the struts is

6 deg, and the geometrical contraction ratio ε is 2.86 in the model without struts. Attachment of 6 mm (type 1), 7.2 mm (type 2) and 9.2 mm-thick (type 3) struts in the throat section (between station 2 and 3) with a width of 14 mm yields $\varepsilon = 5.0$, 5.88, and 8.33, respectively. Type 4 strut is a modification of type 3 and has a streamlined section (tapered by 2 deg) downstream of the trailing edge of the type 3. Each strut has backward-facing steps with a height of 0.8 mm in their shoulders. Dots on the struts in Fig. 3 (and on the side wall in Fig. 4) denote pressure taps. The wedge pressure was measured at seven locations to examine the accuracy in the pressure integration. Pressure behind the backward-facing step and base pressure on the trailing edge were also monitored. The model without the struts is model A, and models with type 1 to type 4 struts are models B, C, D, and E (Table 1).

Drag Measurement Results

The drag coefficients were defined as the drag normalized by the entrance area of the model, A_1, and the dynamic pressure of the freestream q_1. Figure 5 presents the relation between the drag measured by the FMS and the inlet contraction ratios. Standard deviations in the force data are plotted in Fig. 5. For example, averaged $C_{FMS} = 0.331$ and $\sigma = 0.016$ were estimated from eight runs for model B. Most of the error bars are contained in the size of symbols. The drag consists of the support (top wall and support rig) drag and the engine's external and internal drag. The horizontal line ($C_0 = 0.0859 \pm 0.0067$) is the drag caused by the top wall and the support rig. The drag between the horizontal solid and broken lines in Fig. 5 corresponds to the drag on the model's external surfaces. Pressure on the external wall surfaces was monitored at 17 locations. The external drag of the engine ($C_{ext} = 0.0959 \pm 0.0064$) was estimated from the pressure force on the external wedges and the base at the engine exit and on the frictional force acting on the external wet surfaces. The increment from the broken line denotes the internal drag in the models. The results are given in columns D and E in Table 1.

The internal drag increases with the attachment of the struts. For instance, the low-drag coefficient of $C_{int} = 0.075$ in model A without the struts increases to 0.146 in model B and 0.273 in model D. In the engine testing, replacing a 30-mm-thick strut (corresponding to the 6-mm-thick strut here) with the 46-mm-thick strut (the 9.2-mm-thick strut) improved the combustion performance in our engine tests. However, Fig. 5 and Table 1 show that the C_{int} with the thick strut doubles compared with the case of the 30-mm-thick strut and that the doubled C_{int} may annul the improved combustion performance.

Pw Measurement Results

An example contour map of the results from compilation of the Pw data for model E is shown in Fig. 4a, in which the wall pressure

Table 1 Engine configurations and aerodynamic properties in engines in the Mach 6.7 freestream

Model (A)	Strut (B)	ε (C)	C_{FMS} (D)	$C_{int\,I}$ (E)	η_c (F)	η_{p5} (G)	x_p^* mm, (H)	Cd_p (I)	Cd_f (J)	$C_{int\,II}$ (K)	η_{p3} (L)
A	Without	2.86	0.253	0.075	0.959	0.500	599	0.001	0.058	0.060	0.730
B	6.0×151	5.00	0.331	0.146	0.948	0.164	229	0.017	0.116	0.132	0.439
C	7.2×156	5.88	0.339	0.156	0.941	0.107	186	0.036	0.126	0.162	0.362
D	9.2×166	8.33	0.454	0.273	0.931	0.037	126	0.112	0.155	0.268	0.223
E	9.2×246	8.33	0.408	0.227	0.931	0.052	140	0.072	0.172	0.244	0.261

xmin=0.0607120,   MAX=2.4941330o
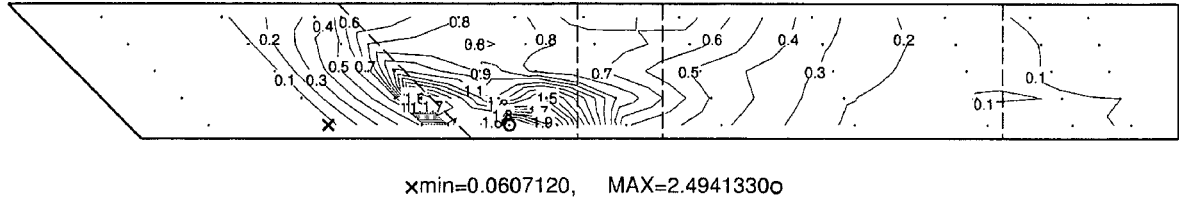
Fig. 4a Wall pressure distributions in model E with the 9.2-mm-thick, long strut.

xmin=0.0013048,   MAX=0.0017153o
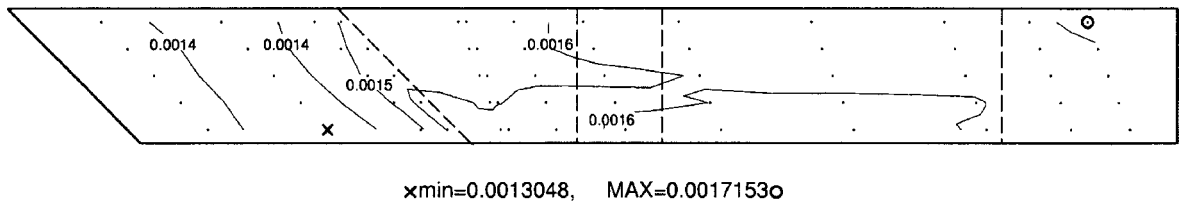
Fig. 4b Distributions of wall friction coefficient evaluated by Fig. 4a.
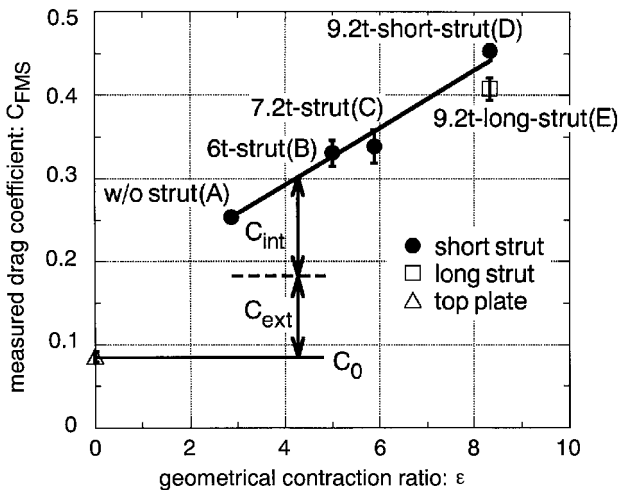
Fig. 5 Total drag measured by force balance, the support rig drag C_0, the external drag, and the internal drag.

is normalized by the dynamic pressure of the Mach 6.7 freestream, for instance, $P_1/q_1 = 0.032$. The wall pressure in the upstream side of inlet is found to be $P/q_1 = 0.061$. Without the strut, the shock wave generated at the leading edge of the sidewall is reflected back between the third and the fourth rows of the measuring ports in the inlet. With the thick strut, the sidewall shock wave, merged with the strut shock wave, impinges just upstream of the third row. In Fig. 4a, however, the discrete shock is smeared by the interpolation process to construct the map. The higher contraction ratio in the inlet ($\varepsilon = 8.33$) increases the maximum pressure to 2.5 (a compression ratio of 80) downstream of the cowl leading edge, which was found to be 10 times higher than maximum pressure in model A without the strut. The reflection of the cowl shock wave on the top wall is observed in the pressure pattern. The high pressure in the combustor decreases toward the nozzle. These Pw data will be discussed later with the swept shock wave analysis.

The internal drag is a sum of the pressure drag and the frictional drag on the internal surface of the engines. The pressure drag is obtained as an integration of the wall pressure shown in Fig. 4a in the axial direction. The frictional drag can be estimated with the shear stress integral if the local Mach number is specified on the surface. The distribution of wall friction coefficient $c_f(M, Re)$ is shown in Fig. 4b, which is calculated from the Pw data in Fig. 4a. To derive Mach number, Reynolds number and c_f in engines, total pressure distributions in engines are now related to the internal drag.

Thrust Functions Across Engines

The engine internal drag can be written using the balance between the thrust functions at stations 1 and 5 defined in Fig. 2:

$$D_{int} \equiv W \cdot \left\{ \int_0^{H_s} (P + \rho u^2) \cdot dy - H_5 \left(P_5 + \rho_5 u_5^2 \right) \right\}$$
$$+ \int_{A_{duct}} \boldsymbol{P}_{duct} \cdot d\boldsymbol{A} + \int_{A_{wet}} (\boldsymbol{Ps} + \boldsymbol{\tau}_s) \cdot d\boldsymbol{A} \quad (1)$$

The first two terms in Eq. (1) express the balance between thrust functions carried in and out by the captured airflow. As shown in Fig. 2, the streamtube entering the inlet expands and generates an additive drag. The third term in Eq. (1) is the additive drag on the free surface of the captured streamtube with an area A_{duct}. The fourth term is the shear force on the wet sidewalls with an area of A_{wet} by the spilled flow. Because the contribution of the spilled flow is contained in the evaluation of engine drag by the force scale and the integration of wall pressure in our experiments, the sum of the third and the fourth terms is added to the engine internal duct drag:

$$D_{add} \equiv \int_{A_{duct}} \boldsymbol{P}_{duct} \cdot d\boldsymbol{A} + \int_{A_{wet}} (\boldsymbol{Ps} + \boldsymbol{\tau}_s) \cdot d\boldsymbol{A} \quad (2)$$

When the height of the dividing streamline of the spilled flow is denoted as H_s, ratio η_c is expressed with the term of the displacement thickness of the boundary layer ingested, δ_1. When the integration

from the wet surface of the top wall to H_s in Eq. (1) is divided into two regions, that inside and that outside of the boundary layer, the balance of thrust function between stations 1 and 5 can be expressed by the boundary-layer thicknesses δ_1 and δ_2:

$$q_1 \cdot C_{\text{int}} = \left\{ [(H_s - \delta)/H]\left(1 + \gamma M_1^2\right) \cdot P_1 \right.$$

$$+ [(\delta - \delta_1 - \delta_2)/H]P_1 \cdot \gamma M_1^2 + D_{\text{add}}/H \cdot W \Big\}$$

$$- P_5\left(1 + \gamma M_5^2\right) \tag{3}$$

A positive C_{int} means a drag by the internal flow. If the pressure ratio P_5/P_1 is expressed by using the total pressure recovery factor η_{p5} at station 5, the drag coefficient of engine duct flow, C_{duct}, can be written as

$$C_{\text{duct}} \equiv C_{\text{int}} - C_{\text{add}} = 2 \cdot (1 - h_1) \cdot \eta_c \cdot \left\{ \left[1 - \frac{h_2}{(1 - h_1) \cdot \eta_c} \right] \right.$$

$$+ \left[1 + \frac{h_1}{(1 - h_1) \cdot \eta_c} \right] \cdot \frac{1}{\gamma M_1^2} \right\}$$

$$- 2 \cdot \left\{ \eta_{p5} \cdot \left\{ \frac{1 + [(\gamma - 1)/2] \cdot M_5^2}{1 + [(\gamma - 1)/2] \cdot M_1^2} \right\}^{-\gamma/(\gamma - 1)} \right.$$

$$\times \left[\frac{1}{\gamma M_1^2} + \left(\frac{M_5}{M_1} \right)^2 \right] \right\} \tag{4}$$

The mass and energy conservation equations yield a relation between η_p, η_c, geometrical contraction ratio ε, total temperature ratio η_{T0}, and Mach number M. Because $\varepsilon_5 = 1$ in this engine, the following relation is obtained:

$$\eta_{p5} = (1 - h_1) \cdot \eta_c \cdot \sqrt{\eta_{T0}}$$

$$\times \frac{M_1}{M_5} \cdot \left(\frac{1 + [(\gamma - 1)/2] \cdot M_5^2}{1 + [(\gamma - 1)/2] \cdot M_1^2} \right)^{[(\gamma + 1)/2 \cdot (\gamma - 1)]} \tag{5}$$

We can specify the η_{T0} or approximate the adiabatic internal flow ($\eta_{T0} = 1$). Substitution of Eq. (5) into Eq. (4) gives the following result about the engine duct drag C_{duct} and Mach number M_5:

$$C_{\text{duct}} = 2 \cdot (1 - h_1) \cdot \eta_c \left[\left\{ \left[1 - \frac{h_2}{(1 - h_1) \cdot \eta_c} \right] \right. \right.$$

$$+ \left[1 + \frac{h_1}{(1 - h_1) \cdot \eta_c} \right] \cdot \frac{1}{\gamma M_1^2} \right\}$$

$$- \sqrt{\eta_{T0}} \cdot \frac{M_1}{M_5} \cdot \left\{ \frac{1 + [(\gamma - 1)/2] \cdot M_5^2}{1 + [(\gamma - 1)/2] \cdot M_1^2} \right\}^{-\frac{1}{2}}$$

$$\times \left\{ \frac{1}{\gamma M_1^2} + \left(\frac{M_5}{M_1} \right)^2 \right\} \right] \tag{6}$$

The force measurement determines C_{int}, and inlet analyses enable the evaluation of C_{add} and η_c. The boundary-layer calibrations in facility nozzles also give h_1, h_2 and Mach number M_1. Thus, the Mach number M_5 is determined with Eq. (6) and η_{p5} is calculated from Eq. (5).

Inlet Flow Analysis

Shock Wave Diagram

To evaluate η_{p5}, we have to specify η_c, C_{add}, h_1, and h_2 as well as C_{int}. Ratio η_c may be measured directly with the air capture experiments. However, η_c and C_{add} can be calculated from shock wave diagrams predicted by an inviscid analysis for swept-back inlets (the swept shock wave analysis[7,11]) assuming an infinitely long wedge.

Table 2 Static pressure rises, Mach number and deflection angles

	Region					
	a	b	c	d	e	f
P/P_1	2.50	5.48	10.8	11.6	33.4	80.0
P/q_1	0.08	0.17	0.35	0.37	1.07	2.56
M_i	5.71	4.96	4.38	4.18	3.28	2.65
θ	1.09	2.37	3.87	4.53	9.28	16.3
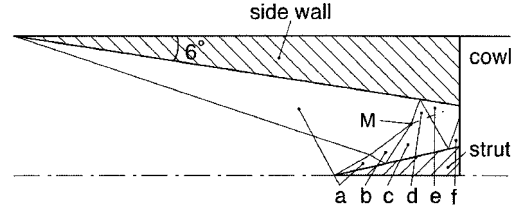
Fig. 6 Shock wave diagrams for model E inlet static pressure, Mach number, and the downward deflection angle summarized.

In the swept shock wave analysis, the flow velocity is broken into vector components normal and tangential to the leading edge. The velocity component tangential to the leading edge remains unchanged. On the contrary, the component perpendicular to the leading edge is reduced at an oblique shock wave by turning when it encounters the wedge, so that the shock wave orientation is determined. The new vectors on the wedge surface are then combined to obtain the velocity and direction of downflow toward the cowl. The calculations must include the change in sweep angle and normal turning angle as the flow crosses each successive shock wave and is turned farther from the top wall.

The shock wave diagram for the inlet with the 9.2-mm-thick strut is shown in Fig. 6. Table 2 shows static pressure rises measured by P_1 and q_1, Mach numbers, and the total downflow angles θ in the individual regions bounded by shock waves and the sidewalls. For instance, when the Mach 6.7 incoming flow is deflected inwardly by 6 deg by the sidewall wedge, the flow is decelerated to $M = 5.71$, resulting in a 2.5-fold increase in the Pw ($P/q_1 = 0.08$). This pressure rise coincides with our Pw measurements. The slightly lower pressure of $P/q_1 = 0.061$ near the lower end of the sidewall in Fig. 4a is due to the end effect by an expansion wave along the sidewall. The swept-back angle of 45 deg in the inlet produces a 1.09 deg downflow deflection.

The shock wave generated at the leading wedge crosses with the strut shock wave to form region b (Fig. 6), with a pressure of $P/P_1 = 5.48$, Mach number $= 4.96$, and the downflow angle $= 2.37$ deg. A right-running wave from the leading edge of the strut merges with the right-running wave reflected back from the strut at a point M (Fig. 6). An expansion wave and a slip line are formed at point M to match the static pressure in region c with that in region d behind the merged wave. The merged wave strikes the sidewall and reflects back to the strut. Region e with a pressure of $P/P_1 = 33.4$ is formed where the airflow is deflected by 9.28 deg downward. Higher Pw is observed in region f on the strut, and the deflection angle of air is calculated to be 16.3 deg.

The right hand boundary in Fig. 6 is the leading wedge of cowl. The cowl produces a strong shock wave with $P/P_1 = 80$ because the deflected air flow is turned back horizontally by the cowl. The inviscid calculation predicts the maximum pressure of $P/q_1 = 2.56$ downstream of Region e. Figure 4a indicates that the region behind the cowl leading wedge reach a higher pressure of $P/q_1 = 2.5$. The impinging points of the shock wave were also surveyed by our oil flow experiments.[12] Thus our Pw experimental data were duplicated and supported theoretically by this swept shock wave analysis.

Air Capture Ratio and Additive Drag

When these results are used, the dividing streamtube of the spilled flow can be constructed by tracing the streamlines impinging at the

cowl leading edge back upstream. Ratio η_c found from this inviscid calculation is given in column F in Table 1. Model A without struts shows a higher η_c of 0.96 and models D and E with the thicker strut have a lower η_c of 0.93. In a real situation with end effects, the boundary layer developed on the sidewalls leaks air on the sidewalls. This leakage through the boundary layer was observed in oil-flow experiments[12] and confirmed in our numerical studies[13] with changing the Reynolds number in the freestream. Our air capture experiments indicated that this end effect through the boundary layer lowered the η_c by about 10%.

The spill flow produces two kinds of additive drag. The first is an additive drag working on the dividing streamtube of the spilled flow. The other is the shear force on the sidewall surfaces wetted by the spilled flow. The static pressure increase due to shock waves is given in Table 2, and the frontal areas with the pressure are found from the intersection of the waves and the flow surfaces. Summation of the resultant axial pressure force on the individual element areas gives the pressure drag on the free boundary and the sidewall. Similarly, the friction contribution to the second additive drag can be estimated from the dynamic pressure and the wall friction coefficient on the wetted sidewalls. The contribution of friction to the total additive drag was found to be less than 10% in our models. The total additive drag was found to be 0.004 (model A) and 0.02 (model D or E) and the contribution of the additive drag to C_{int} was small. This inlet analysis also gives the total pressure loss associated with the shock waves. Ratio η_p in inlets decreases from 85% in the case of model A to 55% in the case of model D or E.

New Method to Evaluate Internal Drag

There are two experimental methods to evaluate C_{int} and η_p at the engine exits by using Eq. (6). The first one is the method to measure D_{int} by the force balance, shown in column E in Table 1. The second way is to evaluate internal drag as the sum of the pressure integration and the shear integration based on the Pw data. These two independent evaluations of η_{p5} have advantages and disadvantages. For instance, the force measurement by balances is direct and reliable. However, it is contaminated by the drag on the supporting strut of engines and the model external surface. The subtraction process $C_{int} = C_{FMS} - (C_0 + C_{ext})$, causes uncertainty in C_{int}, especially for the model with small drag, as shown in a later section. On the other hand, the Pw data do not provide information on the friction drag. An isentropic flow downstream of the inlet has been postulated in strutless engines.[7,8] However, the assumption is not be applicable here because the pressure loss becomes dominant in the engines with the large struts. A new method to estimate the wall shear stress has to be devised.

Pressure Drag Integration

Drag consists of pressure drag and frictional drag. The pressure drag can be evaluated by integrating the pressure distributions as shown in Fig. 4a. Itemizations of pressure drag are represented in Fig. 7 for engines with various struts, in which positive coefficients denote drags worked on converging sections and negative coefficients denote thrust delivered in diverging sections. The total pressure drag Cd_p is given by sums of these positive and negative values and is summarized in column I in Table 1.

In the engine without struts (model A), for instance, the compression surface in the inlet wedges produces a compression drag of 0.06, and the thrust surfaces consisting of the nozzle, the diverging combustor, and the backward-facing steps in the combustor produce a thrust nearly equal to the drag. The drag and the thrust are canceled out, and the total Cd_p becomes small ($Cd_p = 0.001$). The struts produce a drag on the compression surface and a thrust in the diverging sections. Models D and E have the same geometrical contraction ratio of 8.33. However, Cd_p are different because model E has the streamlined strut (type 4 in Fig. 3) and the strut in model D (type 3) has a cutoff tailing base. The strut base in model D produces a strong expansion wave downstream in the engine to decrease thrust in the diverging sections. Consequently, a large Cd_p of 0.112 is found in model D. On the other hand, the streamlined strut increases the thrust in the diverging section to lower the total Cd_p to 0.072.
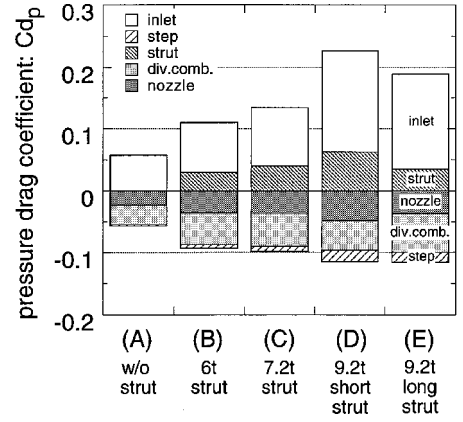

Fig. 7 Itemization of pressure drag: positive values denote drag on compression surfaces.

Wall Shear Stress Integration

Evaluation of the shear force requires assumptions of distributions of c_f and dynamic pressure in the internal flow. We have to devise a method to evaluate the wall shear stress with as few assumptions as possible. In addition, the assumptions should be consistent with the measured Pw data as much as possible.

Wall friction data are correlated with functional forms of $c_f(Re_x, M)$, where Re_x is a local Reynolds number on walls. The local Mach number can be determined if the total pressure distribution in the internal flow is specified. The Mach number and total temperature distributions determine local values of static temperature, and the density and the flow velocity are calculated. Then the local Reynolds number is obtained. Finally, the wall shear stress is calculated by using the extended Frank–Voishel form (see Refs. 14 and 15) for c_f,

$$\tau_{w(x,y)} = \frac{\gamma}{2} \cdot P_w \cdot M^2 \cdot c_f(Re_x, M) \tag{7}$$

$$c_f = \frac{a \cdot \{1 + [(\gamma - 1)/2] \cdot M^2\}^{-0.467}}{(\log Re_x)^{2.58}} \tag{8}$$

where a small value of 0.38 instead of 0.472 is assigned for the constant a in Eq. (8) for the local value of Reynolds number Re. Thus, if $\eta_p(x, y)$ is known, the internal drag, $C_{int} = Cd_p + Cd_f$, can be determined independently of the drag measurement.

An $\eta_p(x)$ averaged on the y–z plane can be defined as

$$\bar{\eta}_p(x) = \int \eta_p(x, y, z) \, dy \, dz \tag{9}$$

because the influence of η_p on the evaluation of Cd_f is weak, as proved later. The $\eta_p(x)$ is a monotonically decaying function with x and any decaying function can be approximated by the exponential function with

$$\bar{\eta}_p(x) = \exp\left(-x/x_p^*\right) \tag{10}$$

The characteristic decay length in total pressure, x_p^* should be consistent with η_{p5} at $x = L$, and η_{p5} can be calculated from the internal drag coefficient C_{int}.

Because η_p does not affect the Reynolds number significantly, the error in the frictional drag caused by the error in η_p appears through the Mach number dependence of c_f in Eq. (8). The following result for the error propagation shows that the influential coefficient of η_p to τ_w is 0.24 at $M = 4$:

$$\Delta \tau_w / \tau_w = (1/\gamma)\{0.533(\gamma - 1) + 2/M^2\} \cdot \Delta \eta_p / \eta_p$$

$$= 0.24 \cdot \Delta \eta_p / \eta_p \quad \text{at} \quad M = 4 \tag{11}$$

Equation (11) states two important facts. The first is that this weak dependence of τ_w on P^0 evaluation supports the approximation
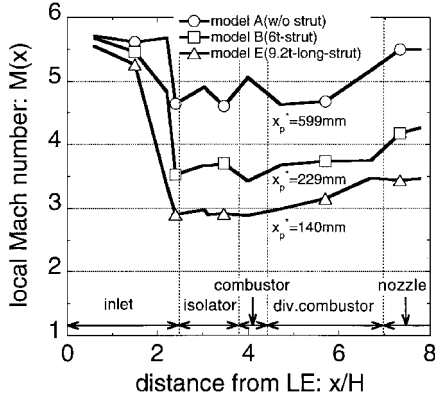
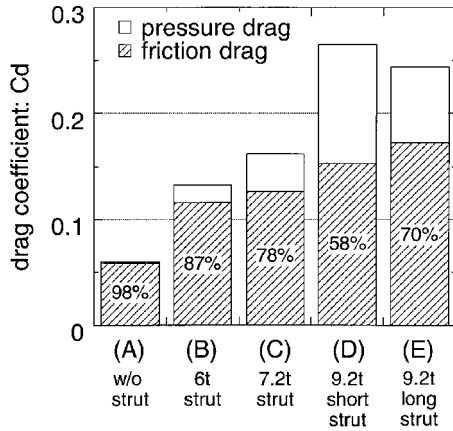**Fig. 8   Mach number distribution in models with the various struts.**

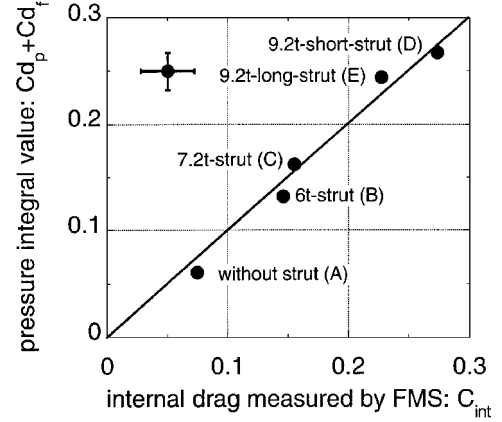**Fig. 9   Internal (pressure and friction) drag evaluated from Pw measurement.**

Fig. 10   Comparison of internal drags evaluated by the method with the force balance and the method based on the Pw measurements.

dependence in Eq. (8). The sum of Cd_p and Cd_f gives another C_{int} (column K), which should be compared with the C_{int} in column E.

These integrations on $Pw(x, y)$ and $\tau_w(x, y)$ make it possible to survey the origins of the pressure and the friction drags. The contributions of Cd_p and Cd_f are summarized in Fig. 9. In model A, the friction drag occupies 98% of the internal drag. The frictional drag is dominant in engines without struts, and it constitutes more than half of internal drag in the model with struts. If models A and D are compared, the Cd_p drastically increases with installing the struts. On the other hand, the dependence of Cd_f on the struts is relatively weak because Cd_f is primarily proportional to the wet surface areas. The large contribution of Cd_f in C_{int} implies that it might be difficult to decrease C_{int} by optimizing the geometry of struts because the geometry affects only the Cd_p .

Comparison of Two Drag Evaluations

The methods for evaluation of C_{int} are compared in Fig. 10, where the horizontal axis denotes the C_{int} measured by the force balance and the vertical axis is the C_{int} evaluated by the pressure and frictional drag integrations. Maximum standard deviations σ in the two methods are indicated in Fig. 10. The maximum deviation in the balance method was evaluated from the datum for model C shown in Fig. 5. The deviation in the Pw method was estimated from the Cd dependence on the choice of individual area elements around discrete pressure taps. Typical standard deviations σ in the two methods are indicated in Fig. 10. Repeatabilities of Pw data at individual pressure taps were within 10%. However, repeatabilities in C_{int} were improved, as shown in Fig. 10, because the integration process averages the local distributions of Pw and τ_w on the internal wall. If these two evaluations are completely consistent with each other, all of the data should be aligned on the straight line inclined by 45 deg. Figure 10 shows good agreements between the two independent evaluations. For the models with the larger struts, the discrepancies were found to be 2% (model D) and 7% (model E). This result justifies our two methods for evaluation of internal aerodynamics and the itemization of drags.

More precise data are provided in columns E and K in Table 1. A relatively large discrepancy in two C_{int} values (25%) is found between 0.075 in column E and 0.060 in column K in model A. The discrepancy in model A and the improved accuracies found in the models with the larger struts suggest that the the error originates from the subtraction process in Fig. 5. As already mentioned, the uncertainties in C_{int} in models with small struts are dominated by the uncertainty of the support rig, C_0. Individual uncertainties in C_0 and C_{ext} yield $C_{int} = 0.075 \pm 0.011 (\sigma)$ for model A. Additional evidence is found from sensitivity of C_{int} to measured data. In model A without struts, the frictional drag constitutes 98% of $C_{int} = 0.060$ and dominates the internal drag. The weak dependence of τ_w on the η_p estimation, as shown in Eq. (11), suggests that the value of $Cd_f = 0.058$ (column J) based on the Pw data is reliable. Thus, we conclude that the force balance data, obtained in

by Eq. (9). The second is that any overestimation of P^0 (underestimation of total pressure loss) yields an overestimation in frictional drag and increases C_{int}. The increase in C_{int} decreases η_{p5} and x_p^*. This dependence of $\tau_w(\eta_{p5})$ ensures the stable convergence of Cd_f evaluation. Thus, the C_{int} can be calculated from the Pw data with any initial guess value for x_p^*. The results of η_{p5} and x_p^* in the models are given in columns G and H in Table 1. The largest x_p^* (the highest η_{p5}) is found to be 599 mm in model A, and the smallest x_p^* is 126 mm in model D for the total model length of 440 mm.

Thus, the total pressure in the models is determined and the local Mach number is calculated with the Pw data. Figure 8 shows the Mach number distributions on the centerline and x_p^* of various engines. The Mach number decreases from $M = 5.5$ in the inlet to $M = 4.6$ at the combustor of model A without struts or $M = 2.9$ in model E with the 9.2-mm-thick strut. The expansion effect and the frictional effect compete with each other and keep the Mach numbers almost constant in the diverging sections.

The distribution of c_f calculated by Eq. (8) is presented in Fig. 4b for model E. In model E, the c_f also varies from 0.0013 in the inlet and 0.0017 in the downstream section of engine. The small c_f results from the Mach number dependence in c_f given by Eq. (8). Figure 8 suggests that the region with higher c_f corresponds to regions covered by lower Mach number flow. In model A without struts, a lower c_f varying from 0.001 to 0.0014 was found.

The local wall stress $\tau_w(x, y)$ is estimated from this $c_f(x, y)$ and $q(x, y) = (\gamma/2) Pw \times M^2$. The frictional drag on the engine wall can be found by integration of the wall shear stress around individual pressure ports. The coefficients of frictional drag evaluated by the integrals are shown in column J of Table 1. The Cd_f increases by attaching thicker and longer struts and varies from 0.058 in model A to 0.172 in model E. This increase of a factor of three in Cd_f is attributed to the wet surfaces of struts and the Mach number

column E, is less accurate for models with small C_{int}, especially for model A.

The C_{int} calculated based on the Pw measurements is adopted to derive the pressure recovery factor η_p in column G and L, Table 1. The η_{p5} at the engine exit decreases from 50% in model A to 4% in model D as shown in column G. The η_{p3} at the throat section can be evaluated from Eq. (10) and is shown in column L. The η_{p3} were found to vary from 73 to 22% in the $M = 6.7$ flow. Because the internal flow geometries are known, all of the flow parameters are calculated with η_{p3}. As reported in Ref. 10, combustion performance, that is, thrust increment by combustion, can be calculated for mixing-control combustion and reaction-control combustion. Subtracting C_{int} from the thrust increment makes the evaluation of the net thrust performance.

Conclusions

The internal flow properties in scramjet engines were investigated by force balance and wall pressure measurements in a Mach 6.7 subscale wind tunnel. Two methods for evaluating the engine internal drag were examined. The following conclusions were derived.

1) The internal drag coefficients C_{int} of scramjet engines were expressed in terms of the air capture ratio, pressure recovery factor, and total temperature ratio. This enables evaluation of the sensitivities of C_{int} to measured experimental values.

2) Shock wave trains in swept-back, side compression-type inlets were analyzed to predict the air capture ratios and the additive drag accompanying the spilled flow. The capture ratio varies from 0.93 to 0.96 in various engine models. Contributions of the additive drag in the internal drag was found to be small (less than 10%).

3) Two independent methods to evaluate engine internal drag were proposed. The first one is the use of force balances, and the second method is based on Pw measurements. In addition to the pressure drag, the friction drag was estimated from the Pw data. The sum of the pressure and friction integrals provided another internal drag. It was found that the frictional drag occupied more than half of the internal drag. The evaluation principle of this friction drag was addressed.

4) Consistency between these methods was examined. Although the force balance was a direct method to measure the engine drag, it was contaminated by drags on external surfaces of engines. Comparative studies of these evaluations concluded that the force balance method was less accurate compared with the Pw method in engines with a small drag.

5) Typical pressure recovery factors were found to be 50% in the engine without struts in the Mach 6.7 freestream. Attachment of the struts decreased η_{p5} to about 16 to 4%. The pressure recovery at the entrance of the combustor varied from 73% in the engine without struts to 22% in the engine with large struts. The

combustion and the net thrust of engines will be estimated based on these flow conditions at the combustors.

References

[1]Chinzei, N., Mitani, T., and Yatsuyanagi, Y., "Scramjet Engine Research at the National Aerospace Laboratory in Japan," *Scramjet Propulsion*, edited by E. T. Curran and S. N. B. Murthy, Vol. 189, Progress in Astronautics and Aeronautics, AIAA, Reston, VA, 2001, pp. 159–222.

[2]Kanda, T., Sunami, T., Tomioka, S., Tani, K., and Mitani, T., "Mach 8 Testing of a Scramjet Engine Model." *Journal of Propulsion and Power*, Vol. 17, No. 1, 2001, pp. 132–138.

[3]Mitani, T., Takahashi, M., Tomioka, S., Hiraiwa, T., and Tani, K., "Analyses and Application of Gas Sampling to Scramjet Engine Testing," *Journal of Propulsion and Power*, Vol. 15, No. 4, 1999, pp. 572–577.

[4]Kobayashi, K., Tomioka, S., Kanda, T., Tani, K., Hiraiwa, T., and Saito, T., "Modified Water-Cooled Scramjet Engine Tested Under M8 Condition," AIAA Paper 2001-3202, July 2001.

[5]Riggins, D. W., "Evaluation of Performance Loss Methods for High-Speed Engines and Engine Components," *Journal of Propulsion and Power*, Vol. 13, No. 2, 1997, pp. 296–304.

[6]Guy, R. W., Torrence, M. G., Sabol, A. P., and Mueller, J. N., "Operating Characteristics of the Langley Mach 7 Scramjet Test Facility," NASA TM-81-929, March 1981.

[7]Voland, R. T., "Methods for Determining the Internal Thrust of Scramjet Engine Modules from Experimental Data," AIAA Paper 90-2340, July 1990.

[8]Mitani, T., Kanda, T., Hiraiwa, T., Igarashi, Y., and Nakahashi, K., "Drags in Scramjet Engine Testing: Experimental and Computational Fluid Dynamics Studies," *Journal of Propulsion and Power*, Vol. 15, No. 4, 1999, pp. 578–583.

[9]Mitani, T., Kobayashi, K., Hiraiwa, T., Tomioka, S., and Masuya, G., "Evaluation of Internal Aerodynamic Performance in Scramjet Engines," AIAA Paper 2001-1885, April 2001.

[10]Mitani, T., Hiraiwa, T., Kouchi, T., and Masuya, G., "Net Thrust Performance in Kinetic-Controlled Scramjet Engines," *Proceedings of the 39th Symposium on Combustion*, Combustion Society of Japan, 2001, pp. 437, 438.

[11]Trexler, C. A., and Souders, S. W., "Design and Performance at a Local Mach Number of 6 of an Inlet for an Integrated Scramjet Concept," NASA TN D-7944, Aug. 1975.

[12]Mitani, T., "Complementary Experiments by the 1/5-subscaled Wind Tunnels of RJTF," National Aerospace Lab., Tech. Rept., Miyagi, Japan, 2002 (to be published).

[13]Kouchi, T., Mitani, T., Kodera, T., and Masuya, G., "Effects of Reynolds Number on Scramjet Inlet Performance," *Proceedings of the Annual Meeting of Northern Section Meeting*, Japan Society for Aeronautical and Space Science, 2002, pp. 47–52.

[14]Rubesin, M. W., Mayden, R. C., and Varga, A. A., "An Analytical and Experimental Investigation of the Skin Friction of the Turbulent Boundary Layer on a Flat Plate at Supersonic Speeds," NACA TN 2305, 1951.

[15]White, F. M., and Christoph, G. H., "A Simple New Analysis of Compressible Turbulent Two-Dimensional Skin Friction Under Arbitrary Condition," U.S. Air Force Flight Dynamics Lab., AFFDL-TR-70-133, Wright–Patterson AFB, OH, 1971.